Applied Catalysis B: Environmental 339 (2023) 123141

Contents lists available at ScienceDirect

Applied Catalysis B: Environmental

journal homepage: www.elsevier.com/locate/apcatb

Construction of Ni_2P-$NiFe_2O_4$ heterostructured nanosheets towards performance-enhanced water oxidation reaction

Yuxin Li [1], Zhe Zhang [1], Ziqi Zhang, Jinghan He, Minggang Xie, Chunguang Li, Haiyan Lu, Zhan Shi [*], Shouhua Feng

State Key Laboratory of Inorganic Synthesis and Preparative Chemistry, College of Chemistry, Jilin University, Changchun 130012, PR China

ARTICLE INFO

Keywords:
Heterostructured nanosheets
In-situ phosphorization
Oxygen evolution reaction (OER)
DFT calculations

ABSTRACT

Water electrolysis represents a promising option for clean hydrogen production, but its overall efficiency is hindered by the sluggish oxygen evolution reaction (OER) with a complex electron transfer process. The construction of heterostructure has emerged as an effective approach to enhance the electrocatalytic performance for OER because of the improvement of exposed active surface and mass/charge transfer. In this work, we report the synthesis of hierarchical nanosheet-structured Ni_2P-$NiFe_2O_4$ as a robust OER catalyst via an annealing treatment and followed by *in-situ* phosphating process. The Ni_2P-$NiFe_2O_4$ electrocatalyst exhibits an overpotential of 305 mV to realize 100 mA cm^{-2} in 1.0 M KOH. Density functional theory calculations further confirm that the construction of heterostructure could optimize adsorption energy of oxygen-containing intermediates and reduce energy barrier during the OER process. This work may provide insights into the electrocatalytic activities of non-noble-metal-based catalysts and present an effective method for the preparation of complex structures.

1. Introduction

Due to the increasingly intractable energy and environmental threats, the development of sustainable and renewable energy conversion and storage systems has attracted extensive attention around the world in an effort to alleviate these serious issues [1–3]. Hydrogen (H_2) has been regarded as a promising alternative to fossil fuels by virtue of its clean nature and high energy density. Water electrolysis, in particular, paves a new way for carbon-free hydrogen production at large scales [4–7]. However, compared with the hydrogen evolution reaction (HER) at the cathode, the oxygen evolution reaction (OER) at the anode has greatly limited the overall water splitting efficiency due to its unique and complex four-step-proton-and-electron transfer process ($4OH^- \rightarrow O_2 + 2\ H_2O + 4e^-$ in base) and the rigid O=O bond formation [8–10]. In addition, the OER process also plays an important role in other renewable energy conversion systems, such as metal-air batteries, solar cells and carbon dioxide reduction [11–13]. Currently, noble metal oxides, such as RuO_2 and IrO_2, are still recognized as the state-of-the-art OER electrocatalysts, but their commercial viability has suffered enormously from their high price, undesirable durability and low abundance in the world [14–17]. Therefore, it is of great urgency and significance to develop efficient and durable non-noble-metal-based electrocatalysts in catalyzing OER reactions to boost the overall efficiency of water electrolysis.

Over the past decades, great efforts have been devoted to the development of cost-effective and low-cost OER electrocatalysts based on non-precious transition metals (Fe, Co, Ni, Mn, etc.), including metal oxides [18,19], sulfides [20,21], phosphides [22,23], nitrides [24] and so on in order to bring down the overpotential required for the OER process. Among different kinds of transition metal oxides, spinel-structured metal oxides (AB_2O_4), such as Co_3O_4, $NiCo_2O_4$, $ZnFe_2O_4$, and $MnFe_2O_4$, which have emerged as attractive and desirable materials towards OER in alkaline solutions owing to their element abundance and rich redox states, have been considered promising replacements of noble-metal-based electrocatalysts [25,26]. Notably, although nickel ferrite ($NiFe_2O_4$) has received substantial attention, the OER electrocatalytic performance is still far from demand, with relatively high overpotential ($\eta > 400$ mV), poor intrinsic activity and limited number of active sites [27]. Recently, many strategies have been employed to enhance the electrocatalytic activity of $NiFe_2O_4$, such as (1) engineering the structures to endow catalysts with enlarged active surface areas and higher hydrophilicity [28]; (2) coating amorphous carbon

* Corresponding author.
E-mail address: zshi@mail.jlu.edu.cn (Z. Shi).
[1] These authors contributed equally to this work.

https://doi.org/10.1016/j.apcatb.2023.123141
Received 6 June 2023; Received in revised form 18 July 2023; Accepted 30 July 2023
Available online 1 August 2023

materials to enhance the electrical conductivity and protect the crystal structures from collapse during the long-time catalytic process [29]; (3) doping other foreign metal or nonmetal elements to modulate electronic structures and distributions [30,31]; (4) decorating the surface of the oxide support with active metal nanoparticles via the exsolution method [32], and (5) employing interfacial engineering method to boost the mass and charge transfer rate within the electrocatalysts, further adjusting the adsorption energies of the intermediates (OH*, OOH* and O*) at the active sites and promoting the whole OER process [33–35].

However, the construction of heterogeneous interfaces generally remains difficult and complex, hindering its practical application on a large scale. In addition, it has been reported that spinel-type metal oxides prepared by general methods are relatively stable thermodynamically, therefore it is difficult to dope other foreign non-metal elements (F, P, S, etc.) by direct *in-situ* synthetic methods (fluorination, phosphorization, sulfidation, etc.), let alone the preparation of hetero-interfaces on them. In order to solve this problem, Liu et al. [36] first introduced oxygen vacancies in $ZnCo_2O_4$ spinel oxide with $NaBH_4$ treatment, and then evaporated fluorine precursor (NH_4F) at low temperature to fill F species into the oxygen vacancies, thus realizing effective non-metal element doping eventually. Liang et al. [37] also reported that the introduction of oxygen vacancies could facilitate phosphorization in the subsequent process because the atom diffusion and phase transformation would be promoted with the existence of vacancies [38,39]. Therefore, considering the works reported previously, the creation of oxygen vacancies prior to the phosphating process could be beneficial for the construction of heterogeneous phase on the relatively stable spinel oxides.

Inspired by the above considerations, in this work, we fabricated the heterostructured nickel phosphide/ferrite (Ni_2P-$NiFe_2O_4$) nanosheet electrocatalyst via a facile synthetic method by combined hydrothermal, annealing and phosphating methods. Benefiting from the electron interactions and mass transfer across the heterointerfaces, the as-prepared Ni_2P-$NiFe_2O_4$ nanosheets showed desirable OER performance in 1.0 M KOH with an overpotential of 305 mV at the current density of 100 mA cm^{-2} and a low Tafel slope of 48.54 mV dec^{-1}. In addition, the electrocatalyst also displayed a high performance in alkaline simulated seawater electrolyte (1 M KOH + 0.5 M NaCl). To gain further insights into the enhanced OER performance, density functional theory calculations were also conducted, which confirmed that the construction of Ni_2P-$NiFe_2O_4$ heterostructure could optimize the *d*-band center and reduce the energy barrier, leading to the enhanced electrocatalytic OER performance.

2. Experimental section

2.1. Chemicals and materials

Nickel nitrate hexahydrate ($Ni(NO_3)_2{\cdot}6\ H_2O$), ferric nitrate nonahydrate ($Fe(NO_3)_3{\cdot}9\ H_2O$), urea (CH_4N_2O) and ammonium fluoride (NH_4F) were obtained from Sinopharm Chemical Reagent Company. Sodium hypophosphite (NaH_2PO_2) and Nafion solution (5 wt%) were acquired via Alfa Aesar. Potassium hydroxide (KOH, 99.99%) and ruthenium (IV) oxide (RuO_2) were purchased from Shanghai Aladdin Biochemical Technology Co Ltd and Shanghai Adamas, respectively. Carbon paper (CP) was bought from TORAY, Japan. All chemicals were used without further purification and all aqueous solutions was prepared using deionized water (DI, 18.2 MΩ·cm^{-1} at 25 °C).

2.2. Preparation of $NiFe(OH)_x$

0.5 g ferric nitrate nonahydrate ($Fe(NO_3)_3{\cdot}9\ H_2O$), 0.5 g nickel nitrate hexahydrate ($Ni(NO_3)_2{\cdot}6\ H_2O$), 0.3 g NH_4F and 1.2 g urea were dissolved in 40 mL deionized water under continuous stirring at room temperature. Then the obtained solution was transferred into a Teflon-lined stainless-steel autoclave and maintained at 100 °C for 20 h. After it cooled to room temperature, the yellow powder was collected via centrifugation and washed with water and ethanol several times, and dried at 80 °C overnight. $Ni(OH)_2$ was prepared by a similar process, without adding ferric nitrated nonahydrate.

2.3. Preparation of Ni_2P, $NiFe_2O_4$, $NiFe_2O_4$/Ni and Ni_2P-$NiFe_2O_4$

Typically, $NiFe(OH)_x$ powder was annealed at 600 °C in Ar atmosphere for 2 h with a heating rate of 5 °C/min. Then the as-prepared sample (named as $NiFe_2O_4$/Ni) was placed downstream in a tube furnace with sufficient amount of NaH_2PO_2 in the upstream, and the *in situ* phosphorization reaction was carried out at 300 °C with a heating speed of 3 °C/min for 2 h under argon protection. The final product was collected after cooling down and denoted as Ni_2P-$NiFe_2O_4$. In addition, Ni_2P was synthesized by the phosphorization treatment of $Ni(OH)_2$ at 300 °C for 2 h and $NiFe_2O_4$ was prepared by annealing $NiFe(OH)_x$ at 600 °C in air for 2 h.

2.4. Material characterizations

Powder X-ray diffraction (XRD) patterns of the synthesized composites were conducted on Bruker D8 (Cu Kα radiation, λ = 1.5418 Å). To observe the morphology of the samples, scanning electron microscopy (SEM) images were collected with the operating voltage of 3 kV on a JEOL JSM-7800 F. Transition electron microscopy (TEM) images and high-resolution TEM (HR-TEM) images were obtained with a Philips-FEI Tecnai G2S-Twin microscope equipped with a field emission gun operating at 200 kV. The surface electronic states and chemical composition of the as-prepared samples were characterized by X-ray photoelectron spectroscopy (XPS) using Thermo ESCALAB 250. Nitrogen adsorption-desorption analysis was conducted on ASAP 2020 (Micromeritics instrument, USA) after degassing at 120 °C for 12 h. The specific surface areas of the samples were obtained based on the Brunauer-Emmett-Teller (BET) model. Raman tests were conducted using an inVia (Renishaw Company) instrument with irradiation at 532 nm.

2.5. Electrochemical measurements

Electrochemical measurements were performed on a CHI-760E electrochemical working station (Chenhua Corp., Shanghai, China.) in a three-electrode cell at room temperature. Typically, graphite rod and Hg/HgO (filled with 1.0 M KOH) were used as the counter electrode (CE) and reference electrode (RE), respectively. To prepare the working electrode, a mixed solution of water (125 μL), ethanol (375 μL) and 5 wt % Nafion solution (10 μL) was used as the solvent, and 2.0 mg of the electrocatalyst was dispersed by sonication for at least 30 min, then 63 μL of the suspension was carefully dropped on a piece of carbon paper (1 ×1 cm^2) and dried at room temperature. The catalyst loading was about 0.25 mg cm^{-2}. The commercial RuO_2 electrode was also fabricated by using the same procedure.

The oxygen evolution reaction (OER) tests were measured in 1.0 M KOH. The reversible hydrogen electrode (RHE) converted from Hg/HgO was obtained from the Nernst equation: $E\ (\mathrm{RHE}) = E\ (\mathrm{Hg/HgO}) + 0.059\ \mathrm{pH} + 0.098$. The overpotential (η) was calculated using the formula: $\eta = E\ (\mathrm{RHE}) - 1.23\ \mathrm{V}$. Before the linear sweep voltammetry (LSV) test, the electrochemical activation of CV was performed at a scan rate of 100 mV s^{-1} until the electrodes were stable and the scan rate for the LSV tests was 5 mV s^{-1} with 90% *i*R-compensated. The Tafel slope was obtained from the Tafel equation: $\eta = a \times \log j + b$, where η is the overpotential, j is the current density and a is the Tafel slope. The CV tests with different scan rates (40, 60, 80, 100, 120, 140 mV s^{-1}) were conducted over non-faradaic potential window. The electrochemically active surface area (ECSA) of the catalyst was calculated from the double-layer capacitance (C_{dl}) according to the equation: $\mathrm{ECSA} = C_{dl}/C_s$. In our work, C_s was estimated to be 40 μF cm^{-2}, according to previous literature [13]. The electrochemical impedance spectroscopy (EIS) analysis was performed

at 0.6 V (*vs.* Hg/HgO) with an amplitude of 5 mV in the frequency range of 0.01 Hz-100 kHz. Chronopotentiometry (CP) and CV measurements were performed to evaluate the stability and durability of the electrocatalyst.

2.6. Density functional theory calculations

DFT calculations were conducted using Vienna ab initio simulation package (VASP). The OER under alkaline conditions consists of four elementary reaction steps, involving an electron transfer to the electrode for each step:

$$OH^- + * \rightarrow *OH + e^- \quad (1)$$

$$OH^- + *OH \rightarrow *O + H_2O + e^- \quad (2)$$

$$OH^- + *O \rightarrow *OOH + e^- \quad (3)$$

$$OH^- + *OOH \rightarrow * + O_2 + H_2O + e^- \quad (4)$$

where * represents the surface of the catalysts, and *O, *OH, *OOH are the adsorbed intermediates. More details on the DFT calculations are provided in the ESI.

3. Results and discussion

3.1. Synthesis and characterizations of the pre-catalysts

A facile three-step strategy was employed to prepare the Ni_2P-$NiFe_2O_4$ heterostructured nanosheets, as shown schematically in Fig. 1 A. In a typical experimental procedure, the $NiFe(OH)_x$ sample was initially prepared through the straightforward hydrothermal reaction, where urea was used to regulate the pH value of the solution and then release OH^- and CO_3^{2-} ions, and NH_4F could modulate the morphology of the resulting products [8,40]. Subsequently, the prepared $NiFe(OH)_x$ powder was annealed at 600 °C in Ar atmosphere to yield $NiFe_2O_4$/Ni. Finally, the Ni_2P-$NiFe_2O_4$ composite was synthesized by a low-temperature (300 °C) *in-situ* phosphating process, using NaH_2PO_2 as the phosphorus source to produce phosphine (PH_3) gas [41].

X-ray diffraction (XRD) measurement was first used to characterize the crystal structures of the as-prepared samples. As displayed in Fig. S1, the diffraction peaks of $NiFe(OH)_x$ could be indexed to NiFe-layered double hydroxides (NiFe-LDH, JCPDS Card No. 40–0215) [2]. After the annealing treatment under the protection of Ar gas, the characteristic peaks of the powder showed excellent agreement with $NiFe_2O_4$ (JCPDS Card No. 10–0325) and metallic Ni (JCPDS Card No. 04–0850), while no peak related to NiFe-LDH was observed, confirming the synthesis of $NiFe_2O_4$/Ni [42] (Fig. 1B). The presence of metallic nickel might be attributed to the oxygen evaporation at the relatively high annealing temperature [41]. The surface morphologies of $NiFe(OH)_x$ and $NiFe_2O_4$/Ni were further characterized by scanning electron microscopy (SEM). It could be seen that both $NiFe(OH)_x$ and $NiFe_2O_4$/Ni exhibited similar uniform flowerlike structures stacked by various 2D nanosheets (NSs) with a film thickness of about 100 nm (Fig. S2A-D). The transmission electron microscopy (TEM) image in Fig. S3 also confirmed the nanosheet morphology of $NiFe_2O_4$/Ni. In the HR-TEM image (Fig. S4), the interplanar spacing of 0.250 nm and 0.202 nm matched well with the (311) facet of $NiFe_2O_4$ and the (111) facet of Ni, respectively, which were in good agreement with the XRD results [34,41,43].

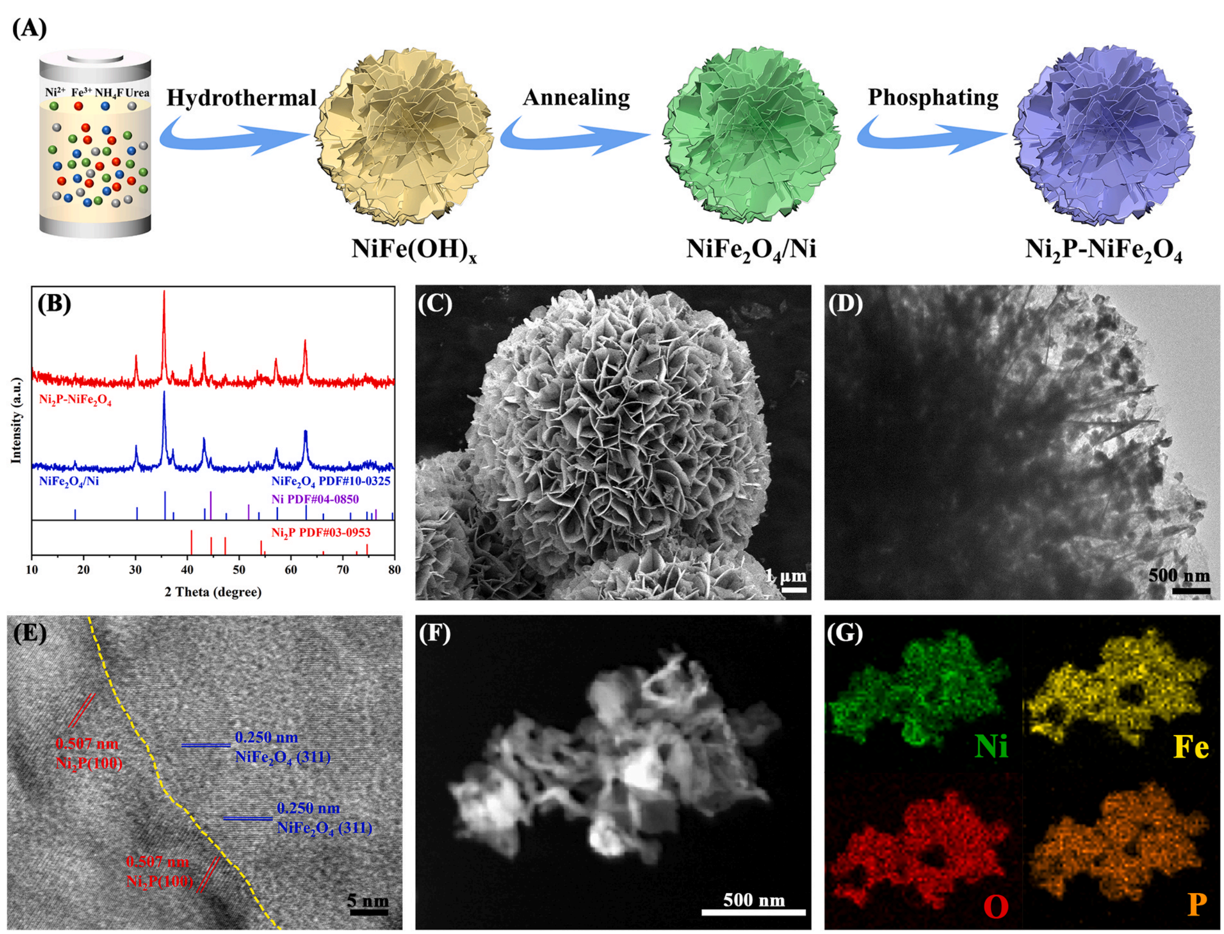

Fig. 1. (A) Schematic illustration of the synthesis procedure for Ni_2P-$NiFe_2O_4$. (B) XRD patterns of $NiFe_2O_4$/Ni and Ni_2P-$NiFe_2O_4$. (C) SEM image, (D) TEM image, (E) HR-TEM image, (F) HAADF-STEM image, and (G) elemental mapping results of Ni_2P-$NiFe_2O_4$.

To shed light on the crystalline composition and the phase information of $NiFe_2O_4$/Ni after phosphating treatment at 300 °C, XRD measurement was first conducted. The XRD pattern (Fig. 1B, Fig. S5) verified that new peaks located at 40.69°, 44.59°, 47.26°, 54.25° and 54.98° could be ascribed to (111), (201), (210), (300) and (211) planes of Ni_2P (JCPDS Card No.03–0953), respectively [44]. The sharp diffraction peaks indicated the high crystalline nature of Ni_2P-$NiFe_2O_4$ and no other phases were introduced during the low-temperature phosphating process. The crystalline compositions and structures of the samples achieved at different phosphating temperatures were also detected by XRD. The results in Fig. S6 demonstrate that lower temperature (250 °C) would result in unsuccessful phosphorization, while higher temperature (400 °C) would influence the crystalline degree of Ni_2P-$NiFe_2O_4$, both of which might hinder the whole electrocatalytic process [6,22]. SEM examination proved that Ni_2P-$NiFe_2O_4$ largely retained the original morphology of $NiFe_2O_4$/Ni and $NiFe(OH)_x$, demonstrating that the phosphating treatment did not affect the architectural features of the composites (Fig. 1C, S2E-F). The samples prepared at other temperatures (250 °C, 350 °C and 400 °C) also displayed the nanosheet-shaped morphology (Fig. S7). It could be seen from the TEM image (Fig. 1D) that compared to $NiFe_2O_4$/Ni, the surface of the nanosheets became rough, which was loaded with some interconnected nanoparticles in the size *ca.* 100–150 nm. It has been reported that such morphology could be helpful for the whole OER process for a rapid reactant supply and a short diffusion pathway [45]. As observed from the HR-TEM image (Fig. 1E), the lattice fringe with a spacing of 0.250 nm could be indexed to the (311) crystal plane of $NiFe_2O_4$ and 0.507 nm to the (100) plane of Ni_2P [34]. Moreover, high-angle annular dark-field scanning transmission electron microscopy (HAADF-STEM) coupled with elemental mapping images confirmed the existence of Ni, Fe, O and P elements and their homogeneous distribution throughout the entire Ni_2P-$NiFe_2O_4$ composite (Fig. 1F, G). The nitrogen adsorption-desorption isotherms of $NiFe_2O_4$/Ni and Ni_2P-$NiFe_2O_4$ are displayed in Fig. S8, which could be considered as a typical type-II isotherm with an evident hysteresis loop, confirming the existence of mesoporous structures in these two composites [45]. The specific Brunauer-Emmett-Teller (BET) surface areas of $NiFe_2O_4$/Ni and Ni_2P--$NiFe_2O_4$ were measured to be 21.14 and 18.98 $m^2\ g^{-1}$, respectively. The decrease in the surface area might be attributed to the collapse of some pores during the low-temperature phosphating process [22,46]. Besides, we employed the most common Barrett-Joyner-Halenda (BJH) model to calculate the pore size distribution of Ni_2P-$NiFe_2O_4$, as shown in Fig. S9A. The porous Ni_2P-$NiFe_2O_4$ nanosheets had mesopore peaks and macropore peaks in the range of 10–70 nm. The porous structure could also be proved by the TEM image in Fig. S9B, C. It has been reported that such mesoporous structures would expose more active sites, thus promoting the electrocatalytic process [27,47].

X-ray photoelectron spectroscopy (XPS) measurement was conducted to probe into the chemical compositions and surface electronic properties of Ni_2P-$NiFe_2O_4$, and the control samples ($NiFe_2O_4$ and Ni_2P) were also measured for comparison. The XPS survey spectra of the as-synthesized electrocatalysts are displayed in Fig. S10, suggesting the existence of Ni. Fe, O and P elements with no impurities. As revealed in Fig. 2A, for the high-resolution Ni 2p spectrum of Ni_2P-$NiFe_2O_4$, the two pairs of peaks located at around 855.11 eV/872.87 eV and 856.87 eV/874.96 eV were assigned to Ni^{2+} ($2p_{3/2}$/$2p_{1/2}$) and Ni^{3+} ($2p_{3/2}$/$2p_{1/2}$), respectively. Additionally, two broad peaks centered at 862.08 eV and 880.12 eV were identified as the typical satellite peaks (Sat.) of Ni $2p_{1/2}$ and Ni $2p_{3/2}$ [8,48,49]. Furthermore, the peak located at 853.61 eV corresponded to the Ni-P bond, also confirming the successful formation of Ni_2P phase on $NiFe_2O_4$ [44,50,51]. It is worth noting that the Ni-P peak presented a positive shift (+ 0.5 eV) compared to that of pristine Ni_2P, and the binding energy of Ni 2p also had negative/positive shift after the construction of Ni_2P-$NiFe_2O_4$, indicating electronic interactions and redistribution between Ni_2P and $NiFe_2O_4$ (Fig. 2A) [51]. In particular, the peak area ratio of Ni^{3+}/Ni^{2+} for Ni_2P-$NiFe_2O_4$ was approximately 1.22, much higher than that of $NiFe_2O_4$ (0.76) and Ni_2P (0.74) (Fig. S11-12), demonstrating the decrease in the electron density around Ni species and an increased valence state of Ni after the phosphidation of $NiFe_2O_4$. It has been reported that abundant Ni^{3+} could enhance the

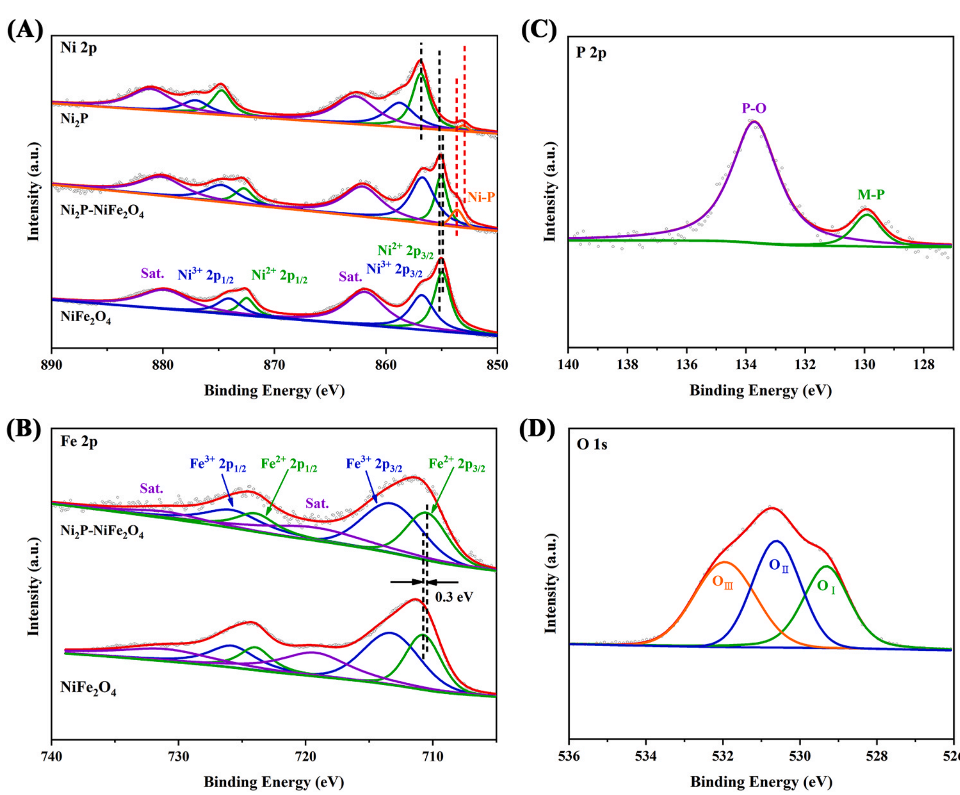

Fig. 2. (A) High-resolution Ni 2p, (B) Fe 2p spectra of the as-prepared samples. (C) P 2p and (D) O 1 s spectra of Ni_2P-$NiFe_2O_4$.

OER performance to a large extent [1,52]. The high-resolution Fe 2p spectrum of Ni_2P-$NiFe_2O_4$ was split into six peaks, which belonged to Fe^{2+} (710.45 eV/723.47 eV) and Fe^{3+} (712.25 eV/725.66 eV), accompanied by two satellite peaks (Sat.) at 714.75 eV and 729.13 eV (Fig. 2B) [34,53]. It could be noticed that the binding energy of Fe 2p orbital moved negatively (- 0.3 eV) and the peak area ratio of Fe^{3+}/Fe^{2+} changed from 1.49 to 1.36 compared with $NiFe_2O_4$, indicating the decrease of Fe^{3+} content and the electron transfer to $NiFe_2O_4$ after the phosphating process [54]. When turning to P 2p spectrum, the peaks at 133.7 eV and 129.9 eV were ascribed to the P species exposed to ambient air and metal-P (M-P) of metal phosphide for Ni_2P-$NiFe_2O_4$, respectively (Fig. 2C) [51]. Finally, the O 1 s spectrum of the Ni_2P-$NiFe_2O_4$ sample was investigated. The high-resolution O 1 s spectrum (Fig. 2D) could be split into three peaks denoted as O_I, O_{II}, and O_{III}. Specifically, O_I peak with the binding energy of 529.3 eV corresponded to lattice oxygen bonded to metals (M-O) [55]. The peak labeled as O_{II} at 530.6 eV was attributed to the hydroxyl groups on metal, whereas O_{III} at ~532.1 eV originated from water molecules (H_2O) absorbed on the surface [56,57]. In summary, the above XPS results indicated that the formation of the Ni_2P-$NiFe_2O_4$ heterostructure could lead to electron interactions and redistribution at the interfaces, which might further improve its electrocatalytic performance.

3.2. Electrocatalytic performance for OER in alkaline media

To evaluate the electrocatalytic oxygen evolution properties of the prepared samples, the as-synthesized catalysts were evenly spread onto 1×1 cm^2 carbon paper and then used as the working electrodes in 1.0 M KOH solution (Fig. 3). All catalysts were tested under the same conditions. Initially, in order to explore the effect of the synthetic temperature, we measured the OER electrocatalytic performances of Ni_2P-$NiFe_2O_4$ prepared at different phosphating temperatures (250 °C, 300 °C, 350 °C and 400 °C). The results revealed that the sample prepared at 300 °C (Ni_2P-$NiFe_2O_4$-300 °C) was optimal for OER (Fig. S13). Therefore, the following study primarily focused on this sample. According to the linear sweep voltammetry (LSV) curves with *i*R-correction in Fig. 3A, the overpotentials of Ni_2P-$NiFe_2O_4$ to reach the current densities of 10 mA cm^{-2}, 50 mA cm^{-2} and 100 mA cm^{-2} were 255 mV, 287 mV and 305 mV, respectively, which were much lower than those of Ni_2P, $NiFe_2O_4$, $NiFe_2O_4$/Ni, $NiFe(OH)_x$ and commercial RuO_2 catalyst

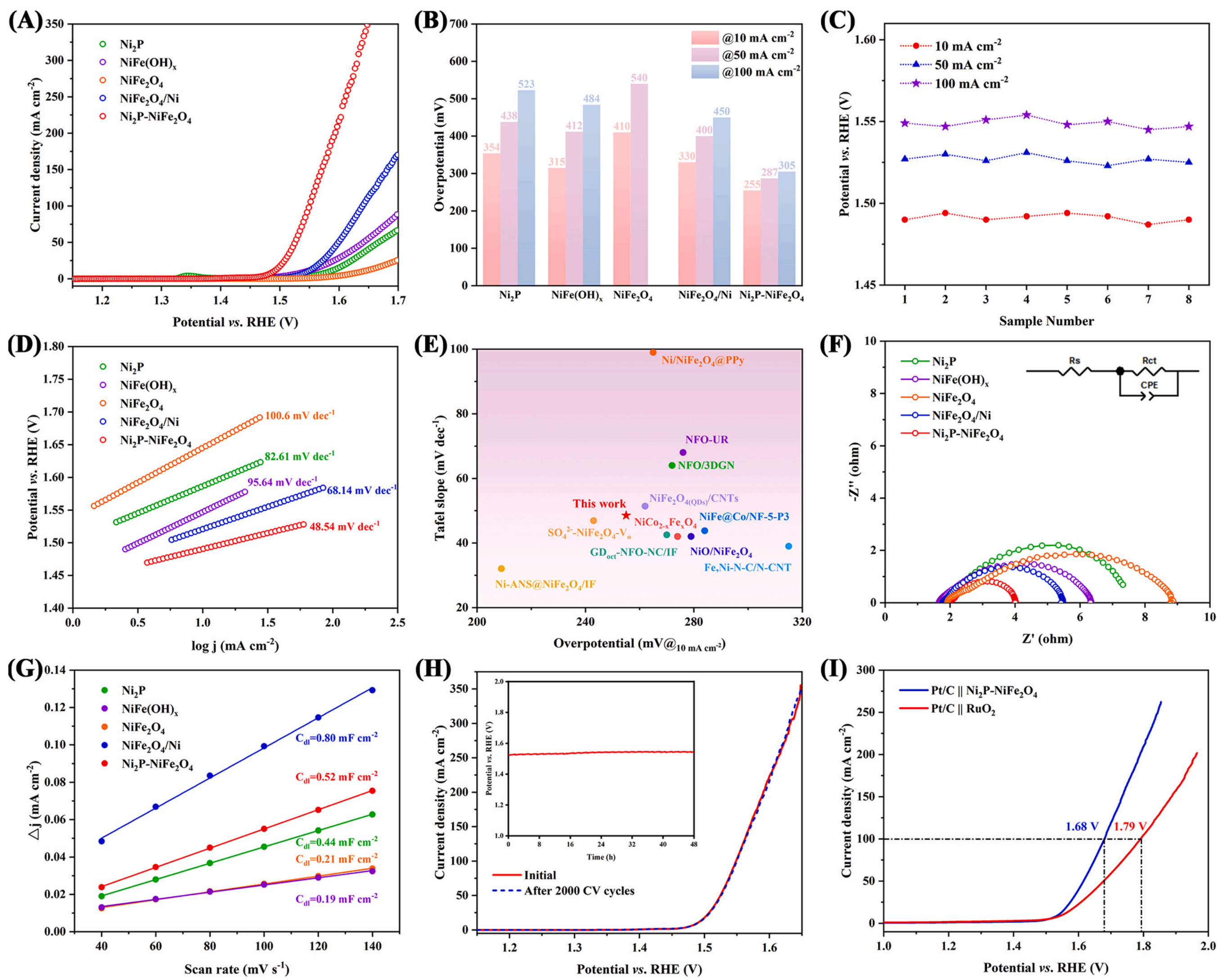

Fig. 3. Electrochemical performances of the as-prepared electrocatalysts in 1.0 M KOH. (A) Polarization curves. (B) The overpotentials to achieve the current densities of 10, 50 and 100 mA cm^{-2} for different samples. (C) Potentials at the current densities of 10, 50 and 100 mA cm^{-2} for Ni_2P-$NiFe_2O_4$. (D) Tafel plots. (E) Overpotentials at 10 mA cm^{-2} and Tafel slopes of some $NiFe_2O_4$-based electrocatalysts reported recently. (F) Nyquist plots of the as-prepared samples. The inset is an equivalent circuit. (G) The fitted C_{dl} at the non-faradaic potential range. (H) LSV curves for Ni_2P-$NiFe_2O_4$ before and after 2000 CV cycles in 1.0 M KOH. Inset: chronopotentiometric durability test for 48 h at 50 mA cm^{-2}. (I) Overall water splitting polarization curves of Pt/C || Ni_2P-$NiFe_2O_4$ and Pt/C || RuO_2.

(Fig. 3B and Fig. S14). With regard to the reproducibility of the prepared Ni_2P-$NiFe_2O_4$, eight working electrodes were synthesized using the same method. No dramatic change was observed for the potentials to reach the current densities of 10, 50 and 100 mA cm^{-2}, which indicated the desirable and superior reproducibility of the prepared Ni_2P-$NiFe_2O_4$ (Fig. 3C). Moreover, the electrocatalytic OER kinetics were determined from Tafel plots. The Tafel slope of 48.54 mV dec^{-1} was achieved for Ni_2P-$NiFe_2O_4$, smaller than those of Ni_2P (82.61 mV dec^{-1}), $NiFe_2O_4$/Ni (68.14 mV dec^{-1}), $NiFe(OH)_x$ (95.64 mV dec^{-1}) and $NiFe_2O_4$ (100.6 mV dec^{-1}), demonstrating a faster kinetics for OER catalysis and more rapid generation of oxygen with the applied potential in alkaline solution (Fig. 3D). The OER performance of the Ni_2P-$NiFe_2O_4$ nanosheets in this work is also competitive to those $NiFe_2O_4$-based OER electrocatalysts reported recently, and the details are shown in Fig. 3E and Table. S1. To gain more understandings of the electrode kinetics during the OER process, electrochemical impedance spectroscopy (EIS) was employed to yield information on the interfacial reactions of the catalysts. After fitting the EIS results by using a simplified equivalent circuit composed of the electrolyte resistance (R_s), a constant phase element (CPE) and the charge transfer resistance (R_{ct}), the R_{ct} values were ranked in the order: Ni_2P-$NiFe_2O_4$ $<$ $NiFe_2O_4$/Ni $<$ $NiFe(OH)_x$ $<$ Ni_2P $<$ $NiFe_2O_4$, suggesting that Ni_2P-$NiFe_2O_4$ had the highest conductivity and fastest charge transfer ability in those synthesized compounds (Fig. 3F and Fig. S15). These results were also in accordance with the LSV information and Tafel slopes.

Furthermore, the electrochemical active surface area (ECSA) is also a crucial descriptor to evaluate the intrinsic performance of the catalysts for water oxidation. Therefore, cyclic voltammetry (CV) measurements at different scan rates in the non-Faradaic range were conducted to achieve the electrochemical double-layer capacitance (C_{dl}) value, which is proportional to ECSA, and the results are depicted in Fig. 3G and Fig. S16A-E. It could be seen that Ni_2P-$NiFe_2O_4$ displayed the C_{dl} value of 0.52 mF cm^{-2}, larger than that of $NiFe(OH)_x$ (0.19 mF cm^{-2}), $NiFe_2O_4$ (0.21 mF cm^{-2}) and Ni_2P (0.44 mF cm^{-2}) but smaller than that of $NiFe_2O_4$/Ni (0.80 mF cm^{-2}), which was also consistent with the BET analysis (Fig. S8). After calculating the ECSA values of the as-prepared electrocatalysts, the current densities of Ni_2P-$NiFe_2O_4$, $NiFe_2O_4$/Ni, $NiFe(OH)_x$, $NiFe_2O_4$ and Ni_2P were normalized to ECSA. Notably, Ni_2P-$NiFe_2O_4$ still exhibited the lowest overpotential to reach the same current density, indicating the most favorable intrinsic activity of Ni_2P-$NiFe_2O_4$ (Fig. S16F). Besides, the MA (mass activity) and SA (area ratio activity) tests also suggested the superior OER catalytic activity of Ni_2P-$NiFe_2O_4$ (Fig. S17). Furthermore, the faradaic efficiency (FE) of Ni_2P-$NiFe_2O_4$ was calculated from the collected oxygen gas during the OER process and the theoretical result, and the value was nearly 100% (Fig. S18). Apart from the high electrochemical activity, stability is another fundamental criterion to estimate the performance of OER catalysts, which was investigated using chronopotentiometry (CP) and cyclic voltammetry (CV) measurements in this study. The chronopotentiometric curve showed negligible increase of the potential after 48 h at the current density of 50 mA cm^{-2}, and the LSV curves before and after conducting 2000 CV cycles almost overlapped (Fig. 3H), indicating the remarkable stability of Ni_2P-$NiFe_2O_4$. Additionally, we also mixed the two samples of Ni_2P and $NiFe_2O_4$ physically, named the final powder as $Ni_2P + NiFe_2O_4$ and compared its electrocatalytic activities with Ni_2P-$NiFe_2O_4$. The results in Fig. S19 demonstrated that $Ni_2P + NiFe_2O_4$ exhibited poorer performance, which might be attributed to the interaction between Ni_2P and $NiFe_2O_4$ was not as strong as the heterostructured Ni_2P-$NiFe_2O_4$ nanosheets, further confirming the fact that the design and construction of proper heterojunction could play an important role in improving the catalytic performance of the electrocatalysts. Finally, a two-electrode configuration electrolyzer was assembled with commercial Pt/C as the cathode and Ni_2P-$NiFe_2O_4$ as the anode for the overall water splitting, and the Pt/C || RuO_2 couple was measured under the same condition as contrast. The polarization curves in Fig. 3I showed that the Pt/C || Ni_2P-$NiFe_2O_4$ couple required 1.538 and 1.68 V to deliver the current densities of 10 and 100 mA cm^{-2}, respectively, better than those of Pt/C || RuO_2 couple (1.55 and 1.79 V). Meanwhile, Pt/C || Ni_2P-$NiFe_2O_4$ also displayed desirable water splitting stability. There was no obvious shift of the cell voltage when working at the current density of 50 mA cm^{-2} (Fig. S20).

3.3. *Investigations on OER mechanism*

In order to investigate the change of the surface chemical state during the catalytic reaction, we performed XPS measurement and compared the spectra of the Ni_2P-$NiFe_2O_4$ catalyst before and after the OER process. From the XPS survey spectrum in Fig. S21A, F 1 s and K 2p signals could be observed obviously, originating from the Nafion solution and KOH electrolyte. For high-resolution Ni 2p spectra, as shown in Fig. 4A, the peaks corresponding to Ni-P bond and Ni^{2+} vanished and the binding energy shifted positively, suggesting the possible surface reconstruction and transformation to (oxy)hydroxide phase after catalysis [13]. Compared with the pristine sample, the binding energy of Fe did not show obvious change but the ratio of Fe^{3+}/Fe^{2+} increased and the spectral intensity decreased (Fig. S21B). These might be due to the oxidation of Fe and possible dissolution of Ni_2P-$NiFe_2O_4$ under the relatively high oxidation potential during the OER process [58]. Moreover, from the high-resolution P 2p spectrum of post-OER Ni_2P-$NiFe_2O_4$, the intensity of Ni-P peak decreased significantly and a broader and weaker peak at around 133 eV could arise from the oxidized P species, which could also prove the surface conversion to (oxy)hydroxides species (Fig. S21C) [59]. Fig. 4B demonstrates that the proportion of the lattice oxygen (M-O) decreased and the hydroxyl oxygen (-OH) in O 1 s spectrum increased after OER tests, also confirming the surface transformation and reconstruction under OER potential. In addition, the signal of oxygen vacancy (O_v) at ~531.7 eV could also be observed, which might be attributed to the defects caused during the surface reconstruction for the OER process [54,60]. We also conducted *in-situ* Raman measurement to probe and confirm the basic phase for OER catalysis (Fig. S22). As depicted in Fig. 4C, the peaks related to $NiFe_2O_4$ phase at 466 cm^{-1} and 555 cm^{-1} for T_{2g} modes, 325 cm^{-1} (E_g) and 690 cm^{-1} (A_{1g}) corresponding to the symmetric and asymmetric stretching vibrations respectively, could be observed between the voltage of 1.2 V and 1.4 V (*vs.* RHE) [61]. When the working potential was above 1.5 V (*vs.* RHE), two peaks at 480 cm^{-1} and 563 cm^{-1} appeared, which were ascribed to the E_g and A_{1g} modes of Ni-O bond in the NiOOH [37]. As for the crystalline structure after the stability tests, XRD measurement was subsequently conducted. It was worth mentioning that the XRD pattern (Fig. 4D) was almost unchanged, suggesting that the crystal heterostructure was not destroyed during the long-time stability tests and the main phases (Ni_2P and $NiFe_2O_4$) remained intact. Apart from the changes of the surface and crystalline compositions, the morphologies of the Ni_2P-$NiFe_2O_4$ catalyst were also characterized. As displayed in the SEM image (Fig. 4E) and TEM image (Fig. S23A), the nanosheet morphology was basically retained after the stability measurement and the lattice fringes of Ni_2P and $NiFe_2O_4$ could also be distinguished clearly in the HR-TEM image (Fig. 4F), which was in good agreement with the XRD result mentioned above. Moreover, a new amorphous phase with thickness of *ca.* 1–5 nm was generated on the surface of the catalyst, which could be regarded as the metal (oxy) hydroxides layer according to the XPS findings of the post-OER electrocatalyst (Fig. S23B). HAADF-STEM image and elemental mapping results of post-OER Ni_2P-$NiFe_2O_4$ also confirmed the existence of Ni, Fe, O and P elements, which matched well with the XRD result (Fig. S24). However, it could be seen that the content of P element had a dramatic decrease, suggesting the possible phase transformation after the OER process. Thus, based on the above XPS, Raman, XRD and TEM results, the (oxy)hydroxides produced on the surface of Ni_2P-$NiFe_2O_4$ were considered to be the real active species for the entire OER process, which also agreed with previously reported work [37,62].

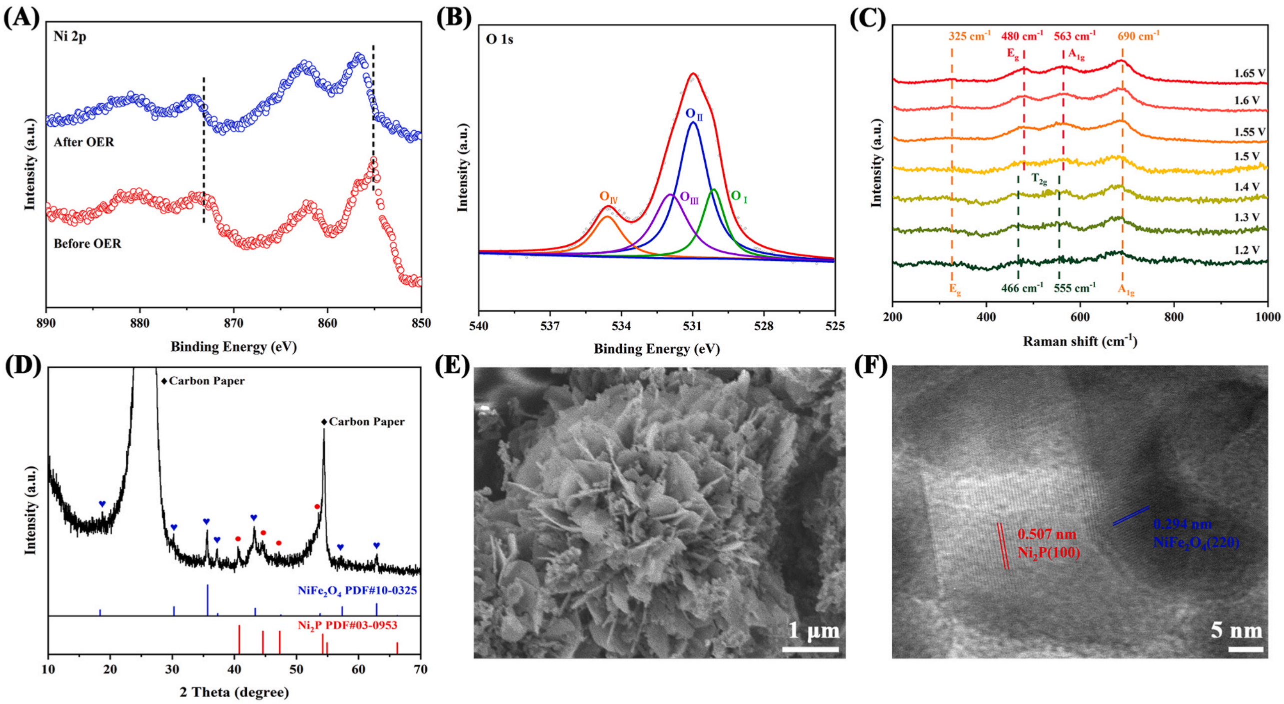

Fig. 4. High-resolution (A) Ni 2p and (B) O 1 s XPS spectra of Ni_2P-$NiFe_2O_4$ after stability test for OER. (C) The *in-situ* Raman spectra of Ni_2P-$NiFe_2O_4$. (D) XRD pattern, (E) SEM image and (F) HR-TEM image of the post-OER Ni_2P-$NiFe_2O_4$ composite.

3.4. DFT calculations

In order to gain more insights into the enhanced OER performance of Ni_2P-$NiFe_2O_4$, density functional theory (DFT) calculations were further performed. Fig. 5A shows the optimized model of the Ni_2P-$NiFe_2O_4$ heterostructure, and other models of Ni_2P and $NiFe_2O_4$ were also established for comparisons (Fig. S25). The (111) facet of $NiFe_2O_4$ and the (001) facet of Ni_2P were selected for their high degree of lattice matching. As displayed in Fig. 5B, the total density of states (DOS) of Ni_2P-$NiFe_2O_4$ was continuous near the Fermi energy level, demonstrating its excellent conductivity. In addition, it could be noticed that the DOS near the Fermi energy level was mainly contributed by Ni, suggesting that Ni might be the main active site for OER process. Furthermore, the *d*-band centers (ε_d) of the Ni atoms of Ni_2P, $NiFe_2O_4$ and Ni_2P-$NiFe_2O_4$ were calculated and the results were shown in Fig. 5C. In general, the closer the *d*-band center is to the Fermi energy level, the higher the antibonding states locate, leading to the stronger interactions and adsorptions of the oxygen-containing intermediates [10,52,55,63,

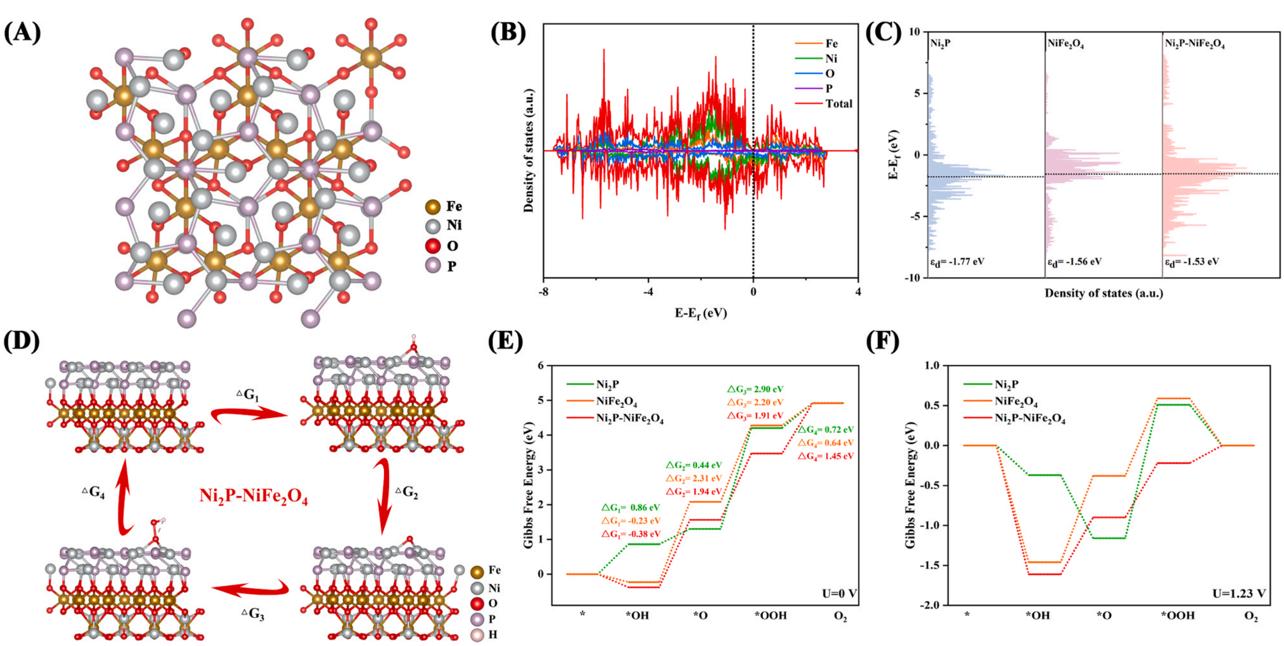

Fig. 5. (A) The optimized atomic structure of Ni_2P-$NiFe_2O_4$. (B) The total density of states (DOS) of Ni_2P-$NiFe_2O_4$. (C) The DOS of Ni site in the Ni_2P, $NiFe_2O_4$ and Ni_2P-$NiFe_2O_4$. (D) The OER cycles for Ni_2P-$NiFe_2O_4$. (E) The energetic pathway of OER in the alkaline solution. (F) The energetic pathway of OER in the alkaline solution under the applied potential of 1.23 V.

64]. Compared to Ni_2P (ε_d=−1.77 eV) and $NiFe_2O_4$ (ε_d= −1.56 eV), after the construction of Ni_2P-$NiFe_2O_4$ heterojunction, the *d*-band center shifted to a higher energy (ε_d= −1.53 eV), which might be attributed to the electron redistribution across the heterogeneous interface.

Subsequently, the free-energy changes of the oxygen reaction intermediates (*OH, *O, *OOH and O_2) corresponding to the four elementary steps were also calculated (Fig. 5D, Fig. S26-27). For $NiFe_2O_4$ and Ni_2P-$NiFe_2O_4$, the generation of *O intermediate from *OH was the rate-determining step (RDS) during the whole OER reaction, and the barriers were calculated to be 2.31 eV and 1.94 eV, respectively. However, the RDS for Ni_2P was the step to form *OOH intermediate ($\triangle G_3$ = 2.9 eV) (Fig. 5E, F). The reduced energy barrier of the RDS indicated that the establishment of Ni_2P-$NiFe_2O_4$ heterojunction could accelerate the OER reaction kinetics, thereby improving electrocatalytic performance. In summary, based on the DFT calculation results, the construction of Ni_2P-$NiFe_2O_4$ heterostructure could optimize the electronic distribution and reduce the energy barrier during the OER process.

3.5. Electrocatalytic performance for OER in simulated seawater

Apart from OER under freshwater condition (1.0 M KOH), we also evaluated the OER performance of the as-prepared electrocatalysts in simulated seawater electrolyte (1.0 M KOH + 0.5 M NaCl). As shown in Fig. 6A, the Ni_2P-$NiFe_2O_4$ electrode required overpotentials of 266 mV, 303 mV and 324 mV to achieve the current densities of 10 mA cm^{-2}, 50 mA cm^{-2} and 100 mA cm^{-2}, respectively, much lower than those of $NiFe(OH)_x$, Ni_2P, $NiFe_2O_4$ and $NiFe_2O_4$/Ni (Fig. 6B). The corresponding Tafel plots in Fig. 6C demonstrated that Ni_2P-$NiFe_2O_4$ exhibited a Tafel slope of 55.79 mV dec^{-1}, smaller than that of $NiFe(OH)_x$ (98.06 mV dec^{-1}), Ni_2P (85.52 mV dec^{-1}), $NiFe_2O_4$ (105.23 mV dec^{-1}) and $NiFe_2O_4$/Ni (70.75 mV dec^{-1}), confirming excellent catalytic activity of Ni_2P-$NiFe_2O_4$. Turning to the charge transfer ability during the OER process in simulated seawater condition, the electrochemical impedance spectroscopy (EIS) was further conducted. As could be seen from Fig. 6D, Ni_2P-$NiFe_2O_4$ possessed the lowest charge transfer resistance (R_{ct}) among the prepared electrocatalysts, accounting for its enhanced OER electrocatalytic activity. Furthermore, the electrochemical double-layer capacitances (C_{dl}) were calculated based on the cyclic voltammetry curves (Fig. 6E, Fig. S28A-E). After normalizing to the effective electrochemical surface area (ECSA), from the j_{ECSA}-normalized polarization curves in Fig. S28F, it can be noticed that Ni_2P-$NiFe_2O_4$ also exhibited the highest inherent catalytic performance. Finally, the stability of Ni_2P-$NiFe_2O_4$ composite in 1 M KOH + 0.5 M NaCl was tested. As displayed in Fig. 6F, no significant fluctuation of the potential at the current density of 50 mA cm^{-2} was observed after 48-hour continuous water oxidation test. In addition, the two LSV curves of Ni_2P-$NiFe_2O_4$ before and after 2000 CV cycles almost coincided with each other in the OER region, indicating that Ni_2P-$NiFe_2O_4$ had not only impressive OER performance but also superior stability. In addition, Ni_2P-$NiFe_2O_4$ also had superior performance to the standard RuO_2 (Fig. S29). Therefore, considering the above testing results, Ni_2P-$NiFe_2O_4$ exhibited excellent and desirable OER electrocatalytic performance in simulated seawater condition.

4. Conclusions

In summary, we successfully fabricated nickel phosphide/ferrite (Ni_2P-$NiFe_2O_4$) heterostructured nanosheets via annealing nickel-iron hydroxides and conducting a controlled phosphating process. Benefiting from its unique nanostructure, more exposed active sites, faster electrolyte/mass diffusion and more favorable intrinsic activity, the obtained Ni_2P-$NiFe_2O_4$ composite showed enhanced water oxidation performance in 1.0 M KOH with an overpotential of 305 mV to achieve the current density of 100 mA cm^{-2} and a low Tafel slope of approximately 48.54 mV dec^{-1}. Meanwhile, DFT calculations results also revealed that the construction of Ni_2P-$NiFe_2O_4$ heterostructure could regulate and optimize the adsorption and desorption energy of the oxygen-containing intermediates during the OER process, therefore improving the intrinsic activity consequently. Noticeably, Ni_2P-$NiFe_2O_4$

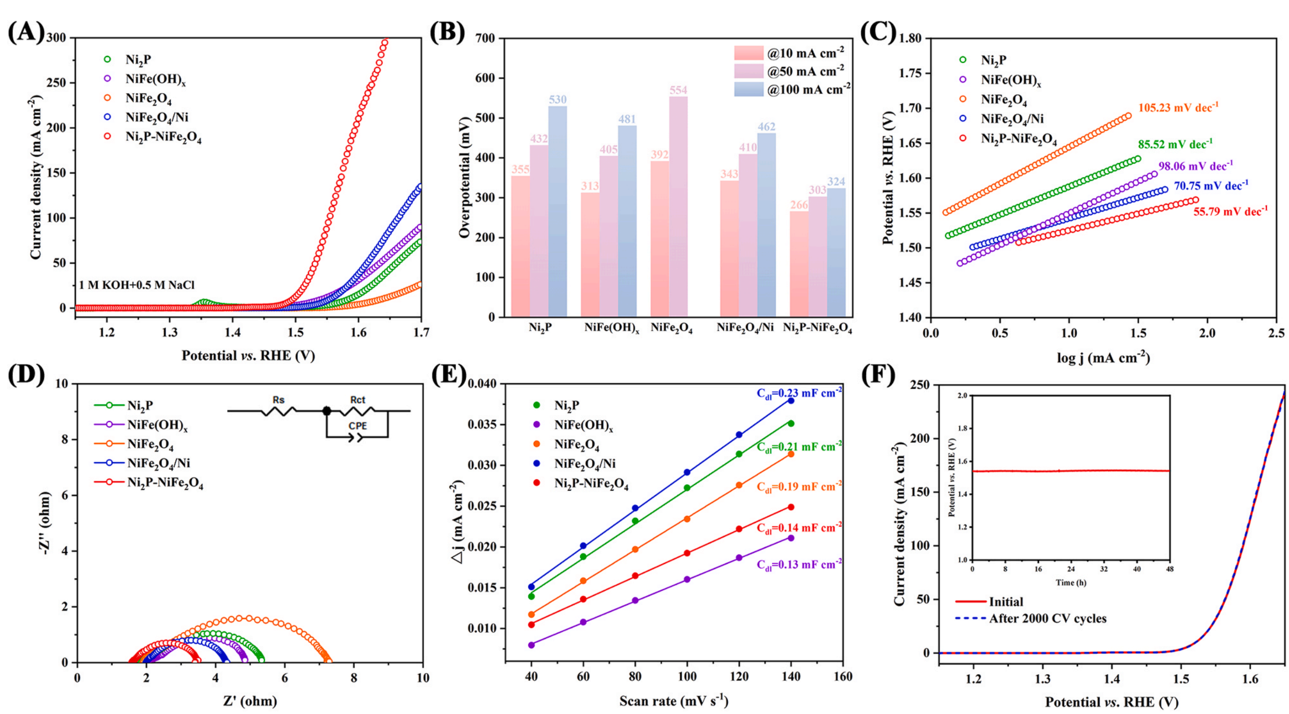

Fig. 6. Electrochemical performances of the as-prepared electrocatalysts in simulated seawater (1.0 M KOH + 0.5 M NaCl). (A) Polarization curves. (B) The overpotentials to achieve the current densities of 10, 50 and 100 mA cm^{-2} for different samples. (c) Tafel plots. (D) Nyquist plots of the as-prepared samples. The inset is an equivalent circuit. (E) The fitted C_{dl} at the non-faradaic potential range. (F) LSV curves for Ni_2P-$NiFe_2O_4$ before and after 2000 CV cycles in 1.0 M KOH + 0.5 M NaCl. Inset: chronopotentiometric durability test for 48 h at 50 mA cm^{-2}.

also showed desirable performance in the simulated seawater condition. We anticipate that this work could provide a new strategy to synthesize non-noble-metal-based effective electrocatalysts for electrochemical water splitting as well as other storage devices and applications for future use.

CRediT authorship contribution statement

Yuxin Li carried out the whole experiment and wrote the paper. **Zhe Zhang** carried out the DFT calculations. **Ziqi Zhang**, **Jinghan He** and **Minggang Xie** conducted the characterizations and performed the analysis of the results. **Chunguang Li**, **Haiyan Lu**, **Zhan Shi** and **Shouhua Feng** provided the resources and supervision.

Declaration of Competing Interest

The authors declare that they have no known competing financial interests or personal relationships that could have appeared to influence the work reported in this paper.

Data availability

Data will be made available on request.

Acknowledgments

This work was financially supported by the National Natural Science Foundation of China (22271114) and 111 Project (B17020). The authors also gratefully acknowledge the financial support by the program for JLU Science and Technology Innovative Research Team (JLUSTIRT).

Appendix A. Supporting information

Supplementary data associated with this article can be found in the online version at doi:10.1016/j.apcatb.2023.123141.

References

[1] S. Huang, Q. Zhang, P. Xin, J. Zhang, Q. Chen, J. Fu, Z. Jin, Q. Wang, Z. Hu, Construction of Fe-doped NiS–NiS_2 heterostructured microspheres via etching prussian blue analogues for efficient water-urea splitting, Small 18 (2022), 2106841.
[2] C. Wu, H. Li, Z. Xia, X. Zhang, R. Deng, S. Wang, G. Sun, NiFe layered double hydroxides with unsaturated metal sites via precovered surface strategy for oxygen evolution reaction, ACS Catal. 10 (2020) 11127–11135.
[3] F. Guo, M. Zhang, S. Yi, X. Li, R. Xin, M. Yang, B. Liu, H. Chen, H. Li, Y. Liu, Metal-coordinated porous polydopamine nanospheres derived Fe_3N-FeCo encapsulated N-doped carbon as a highly efficient electrocatalyst for oxygen reduction reaction, Nano Res. Energy 1 (2022), e9120027.
[4] Y. Xu, R. Wang, Z. Liu, L. Gao, T. Jiao, Z. Liu, Ni_2P/MoS_2 interfacial structures loading on N-doped carbon matrix for highly efficient hydrogen evolution, Green. Energy Environ. 7 (2022) 829–839.
[5] Y. Xu, R. Wang, J. Wang, J. Li, T. Jiao, Z. Liu, Facile fabrication of molybdenum compounds (Mo_2C, MoP and MoS_2) nanoclusters supported on N-doped reduced graphene oxide for highly efficient hydrogen evolution reaction over broad pH range, Chem. Eng. J. 417 (2021), 129233.
[6] T. Xu, D. Jiao, L. Zhang, H. Zhang, L. Zheng, D.J. Singh, J. Zhao, W. Zheng, X. Cui, Br-induced P-poor defective nickel phosphide for highly efficient overall water splitting, Appl. Catal. B Environ. 316 (2022), 121686.
[7] L. Zhang, J. Liang, L. Yue, K. Dong, J. Li, D. Zhao, Z. Li, S. Sun, Y. Luo, Q. Liu, G. Cui, A. Ali Alshehri, X. Guo, X. Sun, Benzoate anions-intercalated NiFe-layered double hydroxide nanosheet array with enhanced stability for electrochemical seawater oxidation, Nano Res. Energy 1 (2022), e9120028.
[8] Y. Zhai, X. Ren, Y. Sun, D. Li, B. Wang, S. (Frank) Liu, Synergistic effect of multiple vacancies to induce lattice oxygen redox in NiFe-layered double hydroxide OER catalysts, Appl. Catal. B Environ. 323 (2023), 122091.
[9] L. Fan, B. Zhang, B.J.J. Timmer, N.V.R.A. Dharanipragada, X. Sheng, C.W. Tai, F. Zhang, T. Liu, Q. Meng, A.K. Inge, L. Sun, Promoting the Fe(VI) active species generation by structural and electronic modulation of efficient iron oxide based water oxidation catalyst without Ni or Co, Nano Energy 72 (2020), 104656.
[10] Q. Wen, K. Yang, D. Huang, G. Cheng, X. Ai, Y. Liu, J. Fang, H. Li, L. Yu, T. Zhai, Schottky heterojunction nanosheet array achieving high-current-density oxygen evolution for industrial water splitting electrolyzers, Adv. Energy Mater. 11 (2021), 2102353.
[11] K. Yao, H. Wang, X. Yang, Y. Huang, C. Kou, T. Jing, S. Chen, Z. Wang, Y. Liu, H. Liang, Metal-organic framework derived dual-metal sites for electroreduction of carbon dioxide to HCOOH, Appl. Catal. B Environ. 311 (2022), 121377.
[12] Y. Yan, R. Zhang, Y. Yu, Z. Sun, R. Che, B. Wei, A.P. LaGrow, Z. Wang, W. Zhou, Interfacial optimization of PtNi octahedrons@Ti_3C_2MXene with enhanced alkaline hydrogen evolution activity and stability, Appl. Catal. B Environ. 291 (2021), 120100.
[13] N. Zhang, Y. Hu, L. An, Q. Li, J. Yin, J. Li, R. Yang, M. Lu, S. Zhang, P. Xi, C.H. Yan, Surface activation and Ni-S stabilization in NiO/NiS_2 for efficient oxygen evolution reaction, Angew. Chem. Int. Ed. 61 (2022), 2207217.
[14] Y. Wu, J. Yang, T. Tu, W. Li, P. Zhang, Y. Zhou, J. Li, J. Li, S. Sun, Evolution of cationic vacancy defects: a motif for surface restructuration of OER precatalyst, Angew. Chem. 133 (2021) 27033–27040.
[15] F. Gao, J. He, H. Wang, J. Lin, R. Chen, K. Yi, F. Huang, Z. Lin, M. Wang, Te-mediated electro-driven oxygen evolution reaction, Nano Res. Energy 1 (2022), e9120029.
[16] Y. Xu, R. Wang, J. Wang, Y. Zhang, T. Jiao, Encapsulation of Fe-CoP with P, N-co-doped porous carbon matrix as a multifunctional catalyst for wide electrochemical applications, J. Energy Chem. 71 (2022) 36–44.
[17] W. Li, Y. Deng, L. Luo, Y. Du, X. Cheng, Q. Wu, Nitrogen-doped $Fe_2O_3/NiTe_2$ as an excellent bifunctional electrocatalyst for overall water splitting, J. Colloid Interface Sci. 639 (2023) 416–423.
[18] F. Hu, D. Yu, M. Ye, H. Wang, Y. Hao, L. Wang, L. Li, X. Han, S. Peng, Lattice-matching formed mesoporous transition metal oxide heterostructures advance water splitting by active Fe–O–Cu bridges, Adv. Energy Mater. 12 (2022), 2200067.
[19] K. Min, M. Hwang, S.E. Shim, D. Lim, S.H. Baeck, Defect-rich Fe-doped Co_3O_4 derived from bimetallic-organic framework as an enhanced electrocatalyst for oxygen evolution reaction, Chem. Eng. J. 424 (2021), 130400.
[20] Z. Wang, S. Shen, Z. Lin, W. Tao, Q. Zhang, F. Meng, L. Gu, W. Zhong, Regulating the local spin state and band structure in Ni_3S_2 nanosheet for improved oxygen evolution activity, Adv. Funct. Mater. 32 (2022), 2112832.
[21] X. Chen, Y. Cheng, Y. Wen, Y. Wang, X. Yan, J. Wei, S. He, J. Zhou, CoP/Fe-Co_9S_8 for highly efficient overall water splitting with surface reconstruction and self-termination, Adv. Sci. 9 (2022), 2204742.
[22] Y. Li, Z. Zhang, M. Xie, C. Li, Z. Shi, S. Feng, A facile templating fabrication of porous CoP nanoparticles towards electrocatalytic oxygen evolution, Appl. Surf. Sci. 583 (2022), 152402.
[23] Q. Wang, Z. Zhang, C. Cai, M. Wang, Z.L. Zhao, M. Li, X. Huang, S. Han, H. Zhou, Z. Feng, L. Li, J. Li, H. Xu, J.S. Francisco, M. Gu, Single iridium atom doped Ni_2P catalyst for optimal oxygen evolution, J. Am. Chem. Soc. 143 (2021) 13605–13615.
[24] J. Huang, Y. Sun, X. Du, Y. Zhang, C. Wu, C. Yan, Y. Yan, G. Zou, W. Wu, R. Lu, Y. Li, J. Xiong, Cytomembrane-structure-inspired active Ni–N–O interface for enhanced oxygen evolution reaction, Adv. Mater. 30 (2018), 1803367.
[25] M. Chen, N. Kitiphatpiboon, C. Feng, Q. Zhao, A. Abudula, Y. Ma, K. Yan, G. Guan, Tuning octahedron sites in $MnFe_2O_4$ spinel by boron doping for highly efficient seawater splitting, Appl. Catal. B Environ. 330 (2023), 122577.
[26] D. Wang, Y. Chen, L. Fan, T. Xiao, T. Meng, Z. Xing, X. Yang, Bulk and surface dual modification of nickel-cobalt spinel with ruthenium toward highly efficient overall water splitting, Appl. Catal. B Environ. 305 (2022), 121081.
[27] L. Huang, D. Chen, G. Luo, Y.R. Lu, C. Chen, Y. Zou, C.L. Dong, Y. Li, S. Wang, Zirconium-regulation-induced bifunctionality in 3D cobalt–iron oxide nanosheets for overall water splitting, Adv. Mater. 31 (2019), 1901439.
[28] J. Liu, H. Yuan, Z. Wang, J. Li, M. Yang, L. Cao, G. Liu, D. Qian, Z. Lu, Self-supported nickel iron oxide nanospindles with high hydrophilicity for efficient oxygen evolution, Chem. Commun. 55 (2019) 10860–10863.
[29] L. Jia, G. Du, D. Han, Y. Wang, W. Zhao, Q. Su, S. Ding, B. Xu, Magnetic electrode configuration with polypyrrole-wrapped Ni/$NiFe_2O_4$ core–shell nanospheres to boost electrocatalytic water splitting, Chem. Eng. J. 454 (2023).
[30] S. Xu, X. Yu, L. Luo, W. Li, Y. Du, Q. Kong, Multiscale manipulating induced flexible heterogeneous V-$NiFe_2O_4$@Ni_2P electrocatalyst for efficient and durable oxygen evolution reaction, Nano Res 15 (2022) 4942–4949.
[31] R. Wei, X. Bu, W. Gao, R.A.B. Villaos, G. MacAm, Z.Q. Huang, C. Lan, F.C. Chuang, Y. Qu, J.C. Ho, Engineering surface structure of spinel oxides via high-valent vanadium doping for remarkably enhanced electrocatalytic oxygen evolution reaction, ACS Appl. Mater. Interfaces 11 (2019) 33012–33021.
[32] X. Guo, L. Yao, X. Hou, X. Wu, Y. Zhang, Q. Zhu, Z. Guo, S. Li, Y. Jiang, S. Feng, K. Huang, An exsolution constructed FeNi/$NiFe_2O_4$ composite: preferential breaking of octahedral metal-oxygen bonds in a spinel oxide, Chem. Sci. 13 (2022) 9440–9449.
[33] X. Li, W.Q. Huang, L.X. Xia, Y.Y. Li, H.W. Zhang, S.F. Ma, Y.M. Wang, X.J. Wang, G. F. Huang, $NiFe_2O_4$/NiFeP heterostructure grown on nickel foam as an efficient electrocatalyst for water oxidation, ChemElectroChem 7 (2020) 4047–4054.
[34] Z. Shao, Q. Zhu, Y. Sun, Y. Zhang, Y. Jiang, S. Deng, W. Zhang, K. Huang, S. Feng, Phase-reconfiguration-induced NiS/$NiFe_2O_4$ composite for performance-enhanced zinc−air batteries, Adv. Mater. 34 (2022), 2110172.
[35] H. Zhong, G. Gao, X. Wang, H. Wu, S. Shen, W. Zuo, G. Cai, G. Wei, Y. Shi, D. Fu, C. Jiang, L.W. Wang, F. Ren, Ion Irradiation inducing oxygen vacancy-rich NiO/$NiFe_2O_4$ heterostructure for enhanced electrocatalytic water splitting, Small 17 (2021), 2103501.
[36] K. Xiao, Y. Wang, P. Wu, L. Hou, Z.Q. Liu, Activating lattice oxygen in spinel $ZnCo_2O_4$ through filling oxygen vacancies with fluorine for electrocatalytic oxygen evolution, Angew. Chem. - Int. Ed. 510006 (2023), 2301408.

[37] C. Kou, J. Zhou, H. Wang, J. Han, M. Han, A. Vomiero, Y. Liu, H. Liang, Boron pretreatment promotes phosphorization of FeNi catalysts for oxygen evolution, Appl. Catal. B Environ. 330 (2023), 122598.
[38] L. Li, T. Meng, J. Wang, B. Mao, J. Huang, M. Cao, Oxygen vacancies boosting lithium-ion diffusion kinetics of lithium germanate for high-performance lithium storage, ACS Appl. Mater. Interfaces 13 (2021) 24804–24813.
[39] X. Wang, J. Liu, Y. Hu, R. Ma, J. Wang, Oxygen vacancy-expedited ion diffusivity in transition-metal oxides for high-performance lithium-ion batteries, Sci. China Mater. 65 (2022) 1421–1430.
[40] L. Yao, H. Zhang, M. Humayun, Y. Fu, X. Xu, C. Feng, C. Wang, Constructing nanoporous crystalline/amorphous $NiFe_2O_4$/NiO electrocatalyst for high efficiency OER/UOR, J. Alloy. Compd. 936 (2023), 168206.
[41] Z. Zhou, Y. Kong, H. Tan, Q. Huang, C. Wang, Z. Pei, H. Wang, Y. Liu, Y. Wang, S. Li, X. Liao, W. Yan, S. Zhao, Cation-vacancy-enriched nickel phosphide for efficient electrosynthesis of hydrogen peroxides, Adv. Mater. 34 (2022), 2106541.
[42] Y. Peng, C. Huang, J. Huang, M. Feng, X. Qiu, X. Yue, S. Huang, Filling octahedral interstices by building geometrical defects to construct active sites for boosting the oxygen evolution reaction on $NiFe_2O_4$, Adv. Funct. Mater. 32 (2022), 2201011.
[43] Q. Li, N. Li, J. An, H. Pang, Controllable synthesis of a mesoporous NiO/Ni nanorod as an excellent catalyst for urea electro-oxidation, Inorg. Chem. Front. 7 (2020) 2089–2096.
[44] Y. Luo, P. Wang, G. Zhang, S. Wu, Z. Chen, H. Ranganathan, S. Sun, Z. Shi, Mn-doped nickel–iron phosphide heterointerface nanoflowers for efficient alkaline freshwater/seawater splitting at high current densities, Chem. Eng. J. 454 (2023), 140061.
[45] X. Yue, X. Qin, Y. Chen, Y. Peng, C. Liang, M. Feng, X. Qiu, M. Shao, S. Huang, Constructing active sites from atomic-scale geometrical engineering in spinel oxide solid solutions for efficient and robust oxygen evolution reaction electrocatalysts, Adv. Sci. 8 (2021), 2101653.
[46] W. Zhu, W. Zhang, Y. Li, Z. Yue, M. Ren, Y. Zhang, N.M. Saleh, J. Wang, Energy-efficient 1.67 V single- and 0.90 V dualelectrolyte based overall water-electrolysis devices enabled by a ZIF-L derived acid–base bifunctional cobalt phosphide nanoarray, J. Mater. Chem. A 6 (2018) 24277–24284.
[47] Y. Jin, H. Wang, J. Li, X. Yue, Y. Han, P.K. Shen, Y. Cui, Porous MoO_2 nanosheets as non-noble bifunctional electrocatalysts for overall water splitting, Adv. Mater. 28 (2016) 3785–3790.
[48] H. Sun, L. Chen, Y. Lian, W. Yang, L. Lin, Y. Chen, J. Xu, D. Wang, X. Yang, M. H. Rümmerli, J. Guo, J. Zhong, Z. Deng, Y. Jiao, Y. Peng, S. Qiao, Topotactically transformed polygonal mesopores on ternary layered double hydroxides exposing under-coordinated metal centers for accelerated water dissociation, Adv. Mater. 32 (2020), 2006784.
[49] C. Li, Z. Zhang, R. Liu, In situ growth of 3D NiFe LDH-POM micro-flowers on nickel foam for overall water splitting, Small 16 (2020), 2003777.
[50] L. Sun, S. Zhao, L. Sha, G. Zhuang, X. Wang, X. Han, Self-supported $Ni_2P/NiMoP_2$ bimetallic phosphide with strong electronic interaction for efficient overall water splitting, J. Colloid Interface Sci. 637 (2023) 76–84.
[51] C.F. Li, J.W. Zhao, L.J. Xie, J.Q. Wu, G.R. Li, Fe doping and oxygen vacancy modulated Fe-Ni_5P_4/NiFeOH nanosheets as bifunctional electrocatalysts for efficient overall water splitting, Appl. Catal. B Environ. 291 (2021), 119987.
[52] Y.C. Zhang, C. Han, J. Gao, J. Wu, X.D. Zhu, J.J. Zou, $Co_{3-x}O_4$/NiO with abundant Ni^{3+} active sites for boosting oxygen evolution reaction, Chem. Eng. J. 446 (2022), 137036.
[53] J. Lv, L. Wang, R. Li, K. Zhang, D. Zhao, Y. Li, X. Li, X. Huang, G. Wang, Constructing a hetero-interface composed of oxygen vacancy-enriched Co_3O_4 and crystalline-amorphous NiFe-LDH for oxygen evolution reaction, ACS Catal. 11 (2021) 14338–14351.
[54] S. Fu, Y. Ma, X. Yang, X. Yao, Z. Jiao, L. Cheng, P. Zhao, Defect and interface engineering of hexagonal $Fe_2O_3/ZnCo_2O_4$ n-n heterojunction for efficient oxygen evolution reaction, Appl. Catal. B Environ. 333 (2023), 122813.
[55] J. Zhang, J. Qian, J. Ran, P. Xi, L. Yang, D. Gao, Engineering lower coordination atoms onto NiO/Co_3O_4 heterointerfaces for boosting oxygen evolution reactions, ACS Catal. 10 (2020) 12376–12384.
[56] S. Liu, H. Zhang, E. Hu, T. Zhu, C. Zhou, Y. Huang, M. Ling, X. Gao, Z. Lin, Boosting oxygen evolution activity of NiFe-LDH using oxygen vacancies and morphological engineering, J. Mater. Chem. A 9 (2021) 23697–23702.
[57] Y. Li, F.M. Li, X.Y. Meng, S.N. Li, J.H. Zeng, Y. Chen, Ultrathin Co_3O_4 nanomeshes for the oxygen evolution reaction, ACS Catal. 8 (2018) 1913–1920.
[58] Q. Han, Y. Luo, J. Li, X. Du, S. Sun, Y. Wang, G. Liu, Z. Chen, Efficient NiFe-based oxygen evolution electrocatalysts and origin of their distinct activity, Appl. Catal. B Environ. 304 (2022), 120937.
[59] W. Song, X. Teng, Y. Niu, S. Gong, X. He, Z. Chen, Self-templating construction of hollow Fe-Co_xP nanospheres for oxygen evolution reaction, Chem. Eng. J. 409 (2021), 128227.
[60] Y. Li, Y. Wu, M. Yuan, H. Hao, Z. Lv, L. Xu, B. Wei, Operando spectroscopies unveil interfacial FeOOH induced highly reactive β-Ni(Fe)OOH for efficient oxygen evolution, Appl. Catal. B Environ. 318 (2022), 121825.
[61] J. Zuo, J. Shen, J. Kang, P. Yan, B. Wang, S. Wang, D. Fu, W. Wang, T. She, S. Zhao, Z. Chen, B-doped $NiFe_2O_x$ based on the activation of peroxymonosulfate for degrading 2,4-dichlorophenoxyacetic acid in water, Chem. Eng. J. 459 (2023), 141565.
[62] Q. Han, Y. Luo, J. Li, X. Du, S. Sun, Y. Wang, G. Liu, Z. Chen, Efficient NiFe-based oxygen evolution electrocatalysts and origin of their distinct activity, Appl. Catal. B Environ. 304 (2022), 120937.
[63] S. Sun, X. Zhou, B. Cong, W. Hong, G. Chen, Tailoring the d-band centers endows $(Ni_xFe_{1-x})_2P$ nanosheets with efficient oxygen evolution catalysis, ACS Catal. 10 (2020) 9086–9097.
[64] Z. Wang, J. Huang, L. Wang, Y. Liu, W. Liu, S. Zhao, Z.Q. Liu, Cation-tuning induced d-band center modulation on Co-based spinel oxide for oxygen reduction/evolution reaction, Angew. Chem. Int. Ed. 61 (2022), 2114696.